PHYSICAL REVIEW B **107**, 115150 (2023)

Single-crystal growth and physical properties of $LaMn_{0.86}Sb_2$

Tianran Yang,[1,*] Liyu Zhang,[1,*] Chin-Wei Wang,[2] Fei Gao,[3] Yuanying Xia,[1] Pengfei Jiang,[4] Long Zhang,[1] Xinrun Mi,[1]
Mingquan He,[1] Yisheng Chai,[1] Xiaoyuan Zhou,[5] Huixia Fu,[5,†] Weijun Ren,[3,‡] and Aifeng Wang[1,§]
[1]*Low Temperature Physics Laboratory, College of Physics and Center of Quantum Materials and Devices, Chongqing University, Chongqing 401331, China*
[2]*National Synchrotron Radiation Research Center, Hsinchu 30077, Taiwan*
[3]*Shenyang National Laboratory for Materials Science, Institute of Metal Research, Chinese Academy of Science, 72 Wenhua Road, Shenyang, 110016, China*
[4]*College of Chemistry and Chemical Engineering, Chongqing University, Chongqing 401331, China*
[5]*Center of Quantum Materials and Devices, College of Physics, Chongqing University, Chongqing 401331, China*

(Received 2 September 2021; revised 7 March 2023; accepted 16 March 2023; published 24 March 2023)

Single crystals of $LaMn_{0.86}Sb_2$ were synthesized via the flux method. Band structure calculation indicates the existence of Dirac dispersion below the Fermi level as expected for the square-net-based materials. Magnetization in combination with neutron diffraction measurements suggests that the magnetic structure below $T_N = 146$ K can be described by a G-type antiferromagnetic structure with a weak spin canting. A spin-flop transition was observed when external magnetic fields were applied parallel to the c axis. Negative magnetoresistance is observed at low temperatures, likely originating from the spin alignment effect. Our results indicate that $LaMn_{1-x}Sb_2$ has Dirac dispersion and a vacancy tunable magnetism, which could be a potential platform for studying the interplay of magnetism, charge transport, and possible topological band.

DOI: 10.1103/PhysRevB.107.115150

I. INTRODUCTION

The layered manganese pnictides $AMnPn_2$ (A = Ca, Sr, Ba, Eu or Yb; Pn = Sb or Bi) family has attracted considerable attention in the field of the topological semimetal [1]. $AMnPn_2$ compounds feature a common layered structure with alternatively stacking of layers of A, $MnPn$, and Pn along the out-of-plane direction. The key structural ingredient of the $AMnPn_2$ compounds is the Pn zigzag/square net, which has been theoretically and experimentally proved to host the Dirac dispersion [1–3]. A layer and the anti-PbO-type $MnPn$ layer mainly serve as buffer layers. Interestingly, the Dirac band is sensitive to the detailed chemical environment of the Pn square net, i.e., the geometry of the A atoms with respect to Pn net [2], and the magnetism of A and $MnPn$ layers [4–7]. Due to the structural diversity, various intriguing quantum transport phenomena have been discovered in $AMnPn_2$ family. Prime examples are quantum Hall effect in $EuMnBi_2$ and $BaMnSb_2$ [4,8], time-reversal-symmetry breaking Weyl fermion in $SrMnSb_2$ and $YbMnBi_2$ [6,7], and giant anisotropic magnetoresistance (AMR) in $EuMnSb_2$ [9]. Therefore, $AMnPn_2$ is a fertile playground for the exploration of topological materials.

Most studies hitherto focused on divalent alkaline/rare earth elements A^{2+} based 112 $A^{2+}MnPn_2$ materials, mainly due to the availability of high-quality single crystals [1]. We note that the trivalent rare earth elements RE^{3+}-based 112 materials, $LaMn_{1-x}Sb_2$, share the same structure with that of $A^{2+}MnPn_2$ [10,11]. Thus, similar physical properties are expected in $LaMn_{1-x}Sb_2$. Although the magnetic properties of $LaMn_{1-x}Sb_2$ polycrystals synthesized by arc melting were reported [10], the magnetotransport properties of $LaMn_{1-x}Sb_2$ remain largely unexplored due to the absence of single crystals.

In this article, we successfully prepared high-quality $LaMn_{0.86}Sb_2$ single crystals using the Sn-flux method. The crystal structure and physical properties of the $LaMn_{0.86}Sb_2$ single crystals were characterized via x-ray powder diffraction (XRPD), first-principles calculation, magnetization, specific heat, and magnetotransport measurements. The refinement of XRPD pattern reveals the existence of Mn vacancies in $LaMn_{0.86}Sb_2$ single crystals. A Dirac-like dispersion at 0.63 eV below Fermi energy is identified by the first-principles calculation. Magnetization of $LaMn_{0.86}Sb_2$ can be explained in the context of a canted AFM magnetic structure with the easy axis along the c axis. A spin-flop transition occurs at 2–4 T when the magnetic field is applied along c axis. The magnetic structure is inferred from the neutron powder diffraction (NPD) measurements performed on $LaMn_{0.78}Sb_2$ which was grown by the Sb-flux method. $LaMn_{0.78}Sb_2$ orders into a G-type AFM structure (a collinear AFM structure in which nearest-neighbor Mn moments in the tetragonal basal plane are antiparallel and successive planes along the c axis are also antiferromagnetically aligned) with an ordered moment of 3.28(4) μ_B/Mn at 3.5 K aligned along the c axis. Therefore, $LaMn_{0.86}Sb_2$ is expected to share a

---

[*] These authors contributed equally to the present work.

[†] hxfu@cqu.edu.cn

[‡] wjren@imr.ac.cn

[§] afwang@cqu.edu.cn

similar magnetic structure with $LaMn_{0.78}Sb_2$, i.e., canted G-type AFM. Negative magnetoresistance (MR) is observed in $LaMn_{0.86}Sb_2$. The correlation between the magnetization and negative MR indicates that the negative MR is induced by the alignment of spins under the magnetic field, which suppresses the spin disorder and spin-dependent carrier scattering.

II. EXPERIMENTAL DETAILS

Single crystals of $LaMn_{0.86}Sb_2$ were grown using the Sn-flux method. La chunks, Mn slices, Sb lumps, and Sn grains were used as starting materials. The starting materials were mixed according to a molar ratio of La:Mn:Sb:Sn = 1:3:6:6. The mixture was subsequently loaded into an alumina crucible and then sealed in an evacuated quartz tube. The sealed quartz tube was heated to 850 °C in 10 h and dwelt for 30 h, and then gradually cooled to 550 °C at a rate of 3 °C/h, where the excess flux was decanted using a centrifuge. Shiny rectangular single crystals with typical dimensions of $3 \times 2 \times 0.2\ \mathrm{mm}^3$ were obtained. As shown in the Supplemental Material [12], $LaMn_{1-x}Sb_2$ single crystals with different x can be successfully grown out by varying the Mn content in the ratio of the starting materials. In order to prepare the large amounts of single crystals required for neutron measurements, we also prepared single crystals by the Sb-flux method, where shiny centimeter-sized single crystals can be obtained. The starting materials were mixed in a molar ratio of La:Mn:Sb = 1:3:6, and the single crystal growth process is similar to the Sn-flux method, only the decanting temperature was changed to 680 °C. Neutron diffraction measurements were performed on Sb-flux-grown single crystals and the rest of the experiments were performed on Sn-flux-grown samples.

The crystal and magnetic structures of $LaMn_{1-x}Sb_2$ single crystals were determined by the x-ray and neutron powder diffraction measurements, respectively. The x-ray powder diffraction (XRPD) data were collected using a PANalytical powder diffractometer (Cu K_α radiation). The neutron powder diffraction (NPD) measurements were performed on high-resolution neutron powder diffractometer ECHIDNA at the OPAL reactor [13], Australian Nuclear Science and Technology Organization (ANSTO). The powder used in neutron diffraction measurements was prepared by pulverizing Sb-flux-grown single crystals (2 g). Rietveld refinements against XRPD and NPD data were performed with FullProf Suite and TOPAS-Academic V6 software, respectively.

To understand the electronic structure of $LaMn_{1-x}Sb_2$, first-principles calculations with spin-orbit coupling (SOC) were taken into account have been performed using Vienna *ab* initio Simulation Package (VASP) in the framework of density functional theory (DFT) [14,15]. An Mn fully occupied tetrahedral $LaMnSb_2$ cell with the lattice constants of $a = 4.377$ Å, $b = 4.377$ Å, and $c = 21.735$ Å were adopted for the theoretical structural model. Note that c is doubled compared to the XRPD results due to the AFM ordering, as shown in Fig. 3(c). The generalized gradient approximation (GGA) of Perdew-Burke-Ernzerhof (PBE) [16] was taken as the exchange-correlation potential. The projector-augmented-wave (PAW) pseudopotential [17] with an energy cutoff of 270 eV was adopted as the basis set. A Γ-centered Monkhorst-Pack k-point mesh of $10 \times 10 \times 2$ was adopted for sampling the first Brillouin zone.

Specific heat and magnetotransport measurements up to 9 T were conducted in a Quantum Design DynaCool Physical Properties Measurement System (PPMS-9T). The angle-dependent measurements were performed by using a home-built insert mounted with a rotator in PPMS-9T. Magnetization was measured with the Quantum Design VSM option of PPMS-9T. Electrical resistivity ρ_{xx} was measured using a standard four-probe method. Hall resistivity ρ_{xy} was measured by a four-terminal technique by switching the polarity of the magnetic field to eliminate contributions from ρ_{xx}. Seebeck coefficient was measured using a home-built probe with one heater, and two-thermometer geometry.

III. RESULTS AND DISCUSSION

A. Crystal and electronic structures

As shown in Fig. 1(a), $LaMn_{1-x}Sb_2$ crystallizes into a tetragonal structure (space group $P4/nmm$), which consists of La, MnSb(1), La, Sb(2) layers alternately stacking along the c axis [10]. Sb(1) and Sb(2) represent the Sb atom located in anti-PbO MnSb(1) layer and Sb(2) square net, respectively. Sb(2) atoms are arranged in a checkerboard-like square net fashion as that in $YbMnSb_2$ [Fig. 1(b)] [18], which is distinct from the zigzag chains found in orthorhombic $A\mathrm{MnSb}_2$ (A = Ca, Sr, Ba, and Eu) [7,19–21]. Figure 1(c) presents the x-ray powder diffraction pattern measured on pulverized Sn-flux grown single crystals, which can be well refined by the $LaMn_{1-x}Sb_2$ structure without discernible impurity. The refined lattice parameters are summarized in Table I, consistent with those reported in polycrystals [10]. The refined chemical composition for Sn-flux-grown single crystals is $LaMn_{0.86}Sb_2$, suggesting the existence of deficiencies on the Mn site. As shown in Supplemental Materials [12], $LaMn_{1-x}Sb_2$ single crystals with $0 \leqslant x \leqslant 0.16$ can be successfully synthesized via the Sn-flux method. Therefore, $LaMn_{1-x}Sb_2$ is adopted as the general chemical formula, and the specific composition, i.e., $LaMn_{0.86}Sb_2$, denotes the detailed single crystal used for physical property measurements.

The Sb square net is located in a similar chemical environment as that in $A^{2+}\mathrm{Mn}Pn_2$, and therefore Dirac dispersion is expected in the electronic structure of $LaMn_{0.86}Sb_2$. First-principles calculation is performed on assumed stoichiometric

TABLE I. Crystallographic parameters and atomic coordinates of $LaMn_{0.86}Sb_2$ extracted from the Rietveld refinements of room temperature powder x-ray diffraction pattern.

X-ray powder diffraction						
Space group: $P4/nmm$; $a = b = 4.37663$ Å, $c = 10.8675$ Å; $R_p = 3.03$, $R_{wp} = 3.95$, GOF = 2.13						
Atom	Wyckoff	x	y	z	Occ.	B_{eq}(Å^2)
La(1)	2c	0.25	0.25	0.23158	1	1.61
Mn(1)	2b	0.75	0.25	0.5	0.859	2.83
Sb(1)	2c	0.25	0.25	0.65588	1	1.86
Sb(2)	2a	0.75	0.25	0	1	1.45

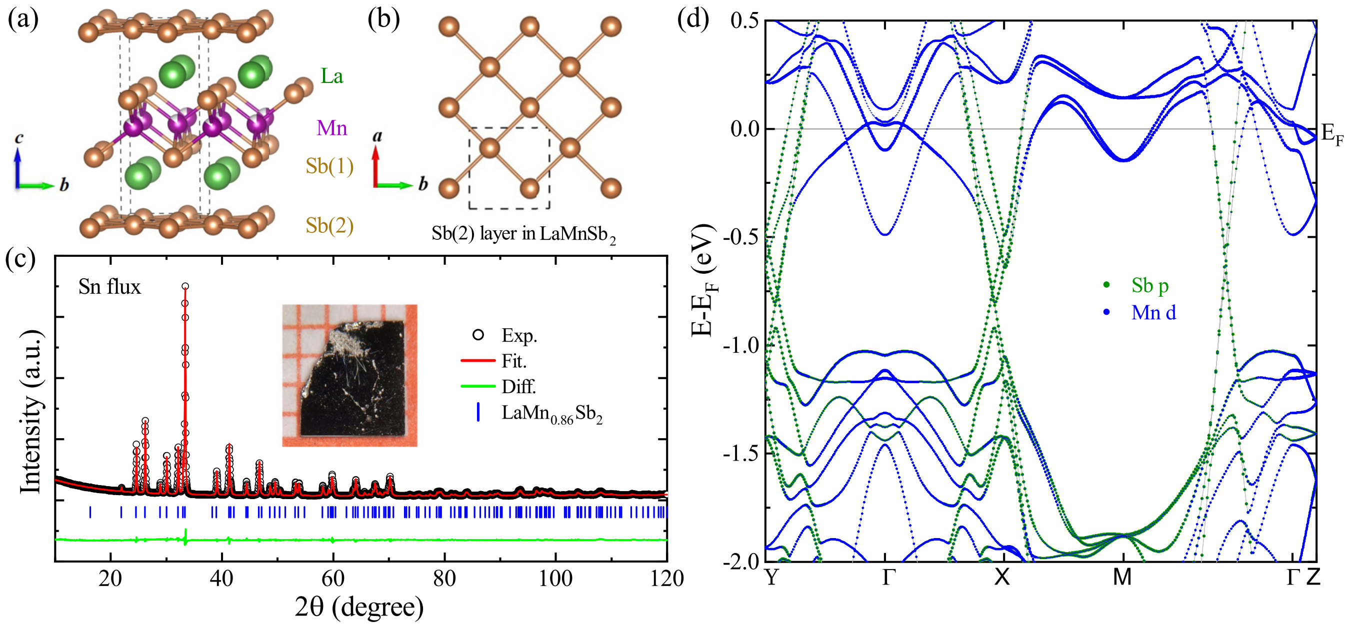

FIG. 1. (a) The crystal structure of $LaMn_{1-x}Sb_2$, in which Sb(1) and Sb(2) denote the Sb bonded with Mn and Sb, respectively. (b) Top view of the Sb square net. (c) Refined x-ray powder diffraction (XRPD) pattern for $LaMn_{0.86}Sb_2$. The inset shows a photograph of $LaMn_{0.86}Sb_2$ single crystal. (c) Band structure for stoichiometric $LaMnSb_2$, which was calculated considering the spin-orbital coupling (SOC) for a G-type AFM structure as shown in Fig. 3(c). Blue and green dots, respectively, represent the states from Mn and Sb.

$LaMnSb_2$ with a G-type AFM ordering to get the electronic structure, and the result is plotted in Fig. 1(d). Multiple bands cross the Fermi level creating the metallic Fermi surface pockets with an average velocity of 3.194×10^5 m/s in combination with both electron-like and hole-like dispersions. The Dirac-like dispersion at 0.63 eV below Fermi level along Γ–M line is derived from *p*-band of Sb as reported in $SrMnSb_2$ and $YbMnSb_2$ [22,23]. These results indicate that $LaMnSb_2$ could be a Dirac semimetal as expected for the square-net materials via adjusting the Fermi level.

B. Magnetization

The temperature dependence of magnetization with $B \parallel c$ ($M_\parallel(T)$) and $B \perp c$ ($M_\perp(T)$) measured at different magnetic fields up to 9 T are plotted in Figs. 2(a) and 2(b), respectively. The subscript $\parallel$ ($\perp$) stands for $B \parallel c$ ($B \perp c$) throughout this paper. As shown by the insets of Figs. 2(a) and 2(b), there is no obvious bifurcation between the magnetization measured in zero-field-cooled (ZFC) and field-cooled (FC) modes, and only ZFC data are shown in this paper. The overall behavior of $M(T)$ is similar to that of $SrMnBi_2$ and $PrMn_{1-x}Sb_2$ [3,24,25], and a magnetic transition at $T_N = 146$ K can be identified, which can be assigned to the antiferromagnetic transition based on the neutron measurements. $M(T)$ exhibits an isotropic behavior at the paramagnetic state. A remarkable anisotropy develops below T_N, where $M_\parallel(T)$ decreases while $M_\perp(T)$ increases with temperature cooling across T_N [Figs. 2(a) and 2(b)]. The weak upturn at T_N for $M_\parallel(T)$ signifies the existence of spin canting [inset of Fig. 2(b)]. The decrease of $M_\parallel(T)$ below T_N is gradually suppressed by increasing the magnetic field, and isotropic $M(T)$ curves are observed when $T \geqslant 5$ T. $M_\parallel(T) < M_\perp(T)$ below T_N implies that the Mn moments orient along *c* axis. Note that a Curie-Weiss tail can be visualized in both $M_\parallel(T)$ and $M_\perp(T)$ at low temperatures, indicative of a remarkable paramagnetic contribution.

Figures 2(c) and 2(d) show the isothermal magnetization, $M(B)$, measured at different temperatures with $B \parallel c$ and $B \perp c$, respectively. No hysteresis was observed in the magnetization loops [Fig. 2(g)]. With increasing magnetic field below T_N, $M_\parallel(B)$ increases linearly first, then steeply after a metamagnetic transition, and eventually, increases with a smaller slope at the high magnetic field, while $M_\perp(B)$ exhibits a typical Brillouin functional form paramagnetic behavior. The maximum moment of $LaMn_{0.86}Sb_2$ is $\sim 0.6\ \mu_B$/f.u. at 9 T [Figs. 2(c) and 2(d)], far from 3.276 μ_B/Mn inferred from neutron measurements. The metamagnetic transition at ~ 3 T for $M_\parallel(B)$ is consistent with the spin-flop transition for an antiferromagnet with moments oriented along the *c* axis. The critical field for spin-flop transition (B_{sf}) is defined as the peak of the first derivative of magnetization with respect to the magnetic field ($dM(B)/dB$) [Fig. 2(e)], which is significantly lower than that in $A^{2+}MnPn_2$, where no metamagnetic transition of Mn sublattice has been observed in a magnetic field up to 35 T [4,26]. The magnetic transitions for $B \parallel c$ are summarized in a phase diagram [Fig. 2(h)] to highlight their temperature and field dependences.

To further understand the magnetization data of $LaMn_{0.86}Sb_2$, we grew a series of $LaMn_{1-x}Sb_2$ single crystals with different Mn vacancies ($x = 0$, 0.14, and 0.16). The data of $LaMnSb_2$, $LaMn_{0.86}Sb_2$ and $LaMn_{0.84}Sb_2$ are shown in the Supplemental Material [12], where systematic evolution of the magnetic properties as a function of Mn vacancies was observed. $LaMnSb_2$ exhibits a typical AFM behavior with $T_N = 172$ K and no Curie-Weiss tail can be observed. As Mn content decreases, T_N decreases to 145 K in $LaMn_{0.86}Sb_2$ and 138 K in $LaMn_{0.84}Sb_2$. The

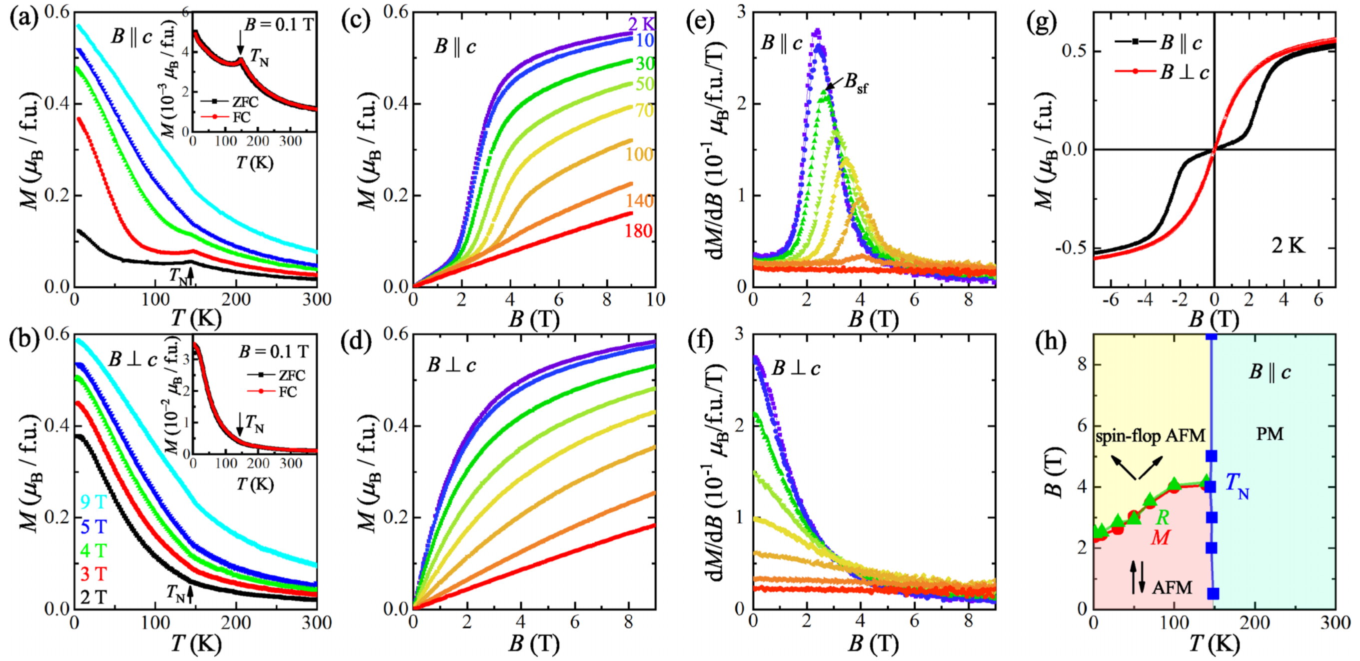

FIG. 2. Temperature-dependent magnetization $M(T)$ for $\mathrm{LaMn_{0.86}Sb_2}$ at various magnetic fields up to 9 T for both $B \parallel c$ (a) and $B \perp c$ (b). The insets show the data of $B = 0.1$ T. Panels (a) and (b) use the same legend. (c–f) Field-dependent magnetization $M(B)$ and corresponding first derivative $dM(B)/dB$ at various temperatures for $B \parallel c$ and $B \perp c$. Panels (c)–(f) use the same legend. (g) Magnetization hysteresis loops at 2 K for $B \parallel c$ and $B \perp c$, respectively. (h) Magnetic phase diagram of $\mathrm{LaMn_{0.86}Sb_2}$ for $B \parallel c$. The criteria for the spin-flop transition are defined as the peaks of the first derivative of magnetization (dM/dB) and resistivity ($d\mathrm{MR}/dB$), respectively, as marked by the arrow in Fig. 2(e) and dashed lines in Fig. 5(b).

saturation behavior of $M(B)$ is achieved in $\mathrm{LaMnSb_2}$, while paramagnetic $M(B)$ curves are observed in $\mathrm{LaMn_{0.86}Sb_2}$ and $\mathrm{LaMn_{0.84}Sb_2}$. Through the comparison of magnetization data between $\mathrm{LaMnSb_2}$, $\mathrm{LaMn_{0.86}Sb_2}$, and $\mathrm{LaMn_{0.84}Sb_2}$, the magnetization of $\mathrm{LaMn_{0.86}Sb_2}$ can be well understood in the framework of an anisotropic antiferromagnet, where the Curie-Weiss tail in $M(T)$ curves and the paramagnetic $M(B)$ curves are induced by the unpaired spins and weakened antiferromagnetic coupling, respectively, both of which are associated with the Mn vacancies.

During the single crystal growth process, we found that $\mathrm{LaMn_{1-x}Sb_2}$ single crystals are easily contaminated with ferromagnetic impurity, even in crystals without discernible impurity phase in the XRPD pattern, which could manifest itself in the magnetization due to the much stronger magnetic signal than the antiferromagnetic matrix. Some of our single crystals include MnSb as the impurity phase in the XRPD pattern, which is a strong ferromagnet with Curie temperature that varies with stoichiometry between 363 K and 587 K [27]. MnSb is also suggested to exist in sister compounds $A\mathrm{MnSb_2}$ (A = Yb, Sr) [27,28]. Thus, the paramagnetism and reported ferromagnetism in $\mathrm{LaMn_{1-x}Sb_2}$ might be induced by the impurity. Another explanation for the origin of the reported ferromagnetism in $\mathrm{LaMn_{1-x}Sb_2}$ polycrystals is the spin canting as those observed in $\mathrm{YbMnBi_2}$ and $\mathrm{Sr_{1-y}Mn_{1-z}Sb_2}$ [6,7].

C. Neutron diffraction

Neutron powder diffraction patterns collected at 150 K, 80 K, and 3.5 K on pulverized Sb-flux-grown $\mathrm{LaMn_{0.78}Sb_2}$ single crystals are shown in Fig. 3(a), and the refined structural and magnetic parameters are summarized in Table II. At 150 K, above the T_N, the diffraction pattern can be fitted to the expected $P4/nmm$ crystal structure. In 3.5 K and 80 K patterns, additional peaks are observed [Fig. 3(b)], indicating the emergence of the long-range magnetic order. These peaks can be indexed with a commensurate wave vector $k = (0, 0, 1/2)$. The BasIreps program is used for the determination of the magnetic structure, which gives the symmetry-constrained models of the magnetic structure. The decomposition of the magnetic representation for the $2b$ site of the space group $P4/nmm$ with a propagation vector of $k = (0, 0, 1/2)$ is as follows: $\Gamma_m(2b) = 1\Gamma_2 + 1\Gamma_5 + 1\Gamma_9 + 1\Gamma_{10}$.

The details of these irreducible representations and the associated basis vectors are tabulated in Table III. For Γ2 and Γ9, the magnetic structures can be described as A-type AFM with ferromagnetic layers stacked antiferromagnetically along c axis, of which the spins are oriented along the c axis (Γ2) and within the ab plane (Γ9), respectively. The magnetic structures of Γ5 and Γ10 are so-called G-type magnetic structures, of which the spin is aligned antiparallelly with its two interlayer and four intralayer nearest neighbors. The difference between the magnetic structures of Γ5 and Γ10 lies in the spin orientation, which is oriented along the c axis for Γ5 and ab plane for Γ10. To extract the proper irreducible representations, the comparison of the magnetic diffraction pattern with various irreducible representations is shown in Fig. 3(b). The observed magnetic diffraction peaks cannot be reproduced with the Γ9 and Γ2 representations. Thus, there are only Γ5 and Γ10 representations that can describe the magnetic diffraction peaks, which correspond

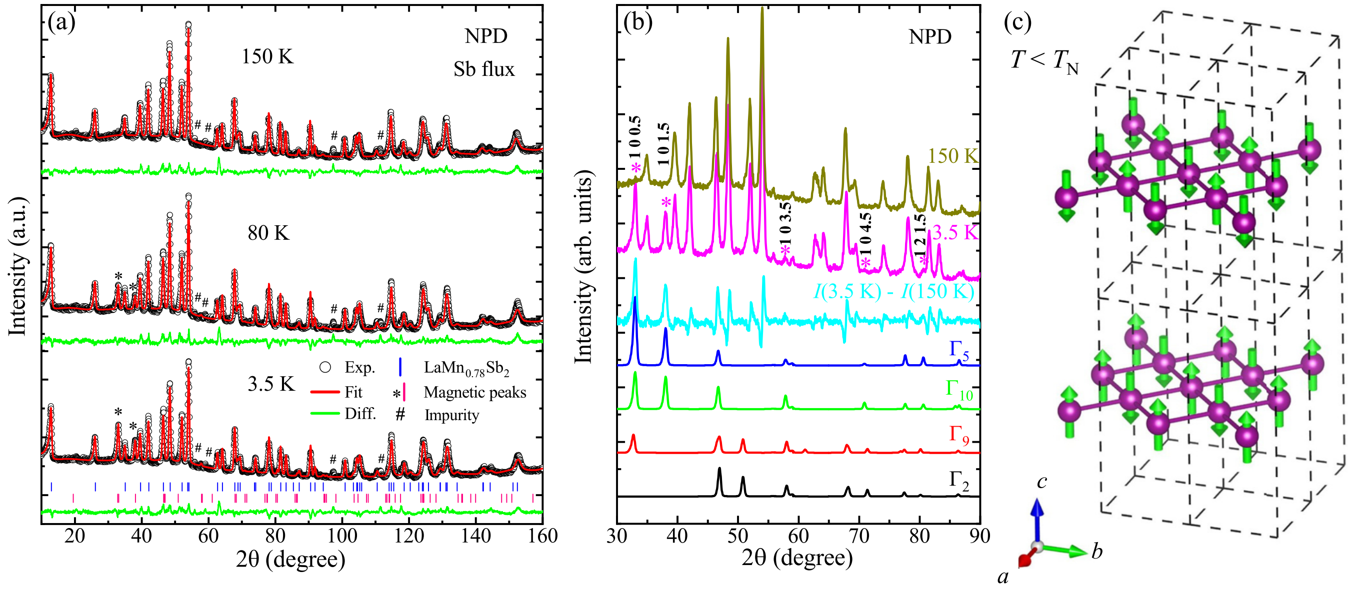

FIG. 3. (a) Refined neutron powder diffraction (NPD) patterns for $LaMn_{0.78}Sb_2$ at various temperatures. Asterisks (*) mark the magnetic Bragg peaks and pound signs (#) mark the impurity. The impurity was not observed in the corresponding XRPD pattern and cannot be indexed by a common impurity phase, i.e., Sb or MnSb. The peak intensities of the impurity do not change with temperature and do not affect the refinements for magnetic structure. (b) The magnified view of the NPD patterns at 150 K, 3.5 K, and their difference $I(3.5\text{ K}) - I(150\text{ K})$ which can be taken as the magnetic diffraction. The diffraction pattern of various irreducible presentations is plotted together for comparison. (c) The magnetic structure of $LaMn_{0.78}Sb_2$, dashed line represents the crystallographic unit cells. The magnetic unit cell is doubled along the c axis with respect to the crystallographic unit cell.

to G-type magnetic structures with moments aligned along c (Γ5) and ab plane (Γ10), respectively. Although magnetic reflections corresponding to Γ5 and Γ10 representations have the same peak positions, Γ5 gives rise to a better description of the peak intensities than Γ10, as reflected by the relative intensities between (1 0 1/2) and (1 0 3/2) peaks [Fig. 3(b)]. Moreover, when we perform the Mn magnetic structure refinements with the Γ5 and Γ10 representations, the obtained R_p factors are 3.7% and 3.9%, respectively. These results indicate that the magnetic diffraction patterns can be best described with the irreducible presentation, Γ5, which is equivalent to the magnetic space group P_c4/ncc (BNS no. 138.528). The magnetic structure corresponding to the Γ5 representation of $LaMn_{0.78}Sb_2$ is displayed in Fig. 3(c), showing a G-type AFM structure with all Mn moments oriented along the c axis, consistent with the magnetization results. The refined Mn moments are 2.44(4) μ_B and 3.28(4) μ_B at 80 K and 3.5 K, respectively. The saturation magnetic moment of ~ 3.3 μ_B is comparable to that of sister compounds $AMnPn_2$ (A = Sr, Ca, Yb; Pn = Sb, Bi) [29,30], but significantly smaller than 5 μ_B expected for the localized Mn^{2+} ($3d^5$, S = 5/2).

The G-type AFM structure was also observed in $SrMnBi_2$ [29], but different from the C-type magnetic structure in $CaMnBi_2$ and $YbMnSb_2$ [28,29]. It was reported that $PrMn_{1-x}Sb_2$ has an identical magnetic wave vector of k= (0, 0, 1/2) with $LaMn_{0.78}Sb_2$, however, the reported magnetic structure contains A-type and G-type arrangement along the c axis and within the ab plane, respectively [24,25], which is the linear combination of Γ2 and Γ10, or the monoclinic magnetic space group C_cca (BNS no. 68.518). For $LaMn_{0.78}Sb_2$, the symmetry allowed canted AFM corresponds to Γ5 + Γ9 representations. As shown in Fig. 3(b), the existence of Γ9 component cannot be resolved by current neutron diffraction measurements, suggesting either the absence of or a very weak spin canting in $LaMn_{0.78}Sb_2$, contrast with the canted AFM suggested by the magnetization measurements for $LaMn_{0.86}Sb_2$. The possible explanation is that the canting in $LaMn_{1-x}Sb_2$ is either too weak to be recognized by neutron measurements or sensitive to the Mn vacancies. Based on the magnetization and neutron measurements, the magnetic structure of $LaMn_{0.86}Sb_2$ is very likely a G-type AFM with a weak canting.

D. Transport properties

Temperature dependence of in-plane electrical resistivity for a $LaMn_{0.86}Sb_2$ single crystal is plotted in Fig. 4(a), which exhibits a metallic behavior with a slope change at $T_N = 146$ K. The slope change is caused by the loss of spin-disorder scattering upon antiferromagnetic ordering. The antiferromagnetic transition is also manifested as a jump in specific heat and a slope change in the Seebeck coefficient [Figs. 4(b) and 4(e)], indicating a bulk intrinsic transition. The room temperature resistivity is 160 $\mu\Omega$ cm, and the residual resistivity ratio (RRR) is estimated to be $\rho(300\text{ K})/\rho\ (2\text{ K}) = 3.3$. RRR is smaller than that of $AMnSb_2$ (A = Sr, Ba, Eu, and Yb) [5,7,18,20], which might be caused by the strong spin disorder scattering.

Hall resistivity and Seebeck coefficient are measured to get insight into the carrier information. $\rho_{xy}(B)$ curves exhibit a slight nonlinear behavior with the positive slope in the temperature range of 2–300 K [Fig. 4(c)], indicating the multiband behavior with dominant hole-type charge carriers. The hole concentration estimated by a single-band linear fitting

TABLE II. The crystal and magnetic structure parameters of $\mathrm{LaMn_{0.78}Sb_2}$ determined by neutron diffraction.

Atom	Wyckoff	x	y	z	Occ.
$T = 150$ K					
Space group: $P4/nmm$; $a = b = 4.3740$ Å, $c = 10.8015$ Å; Magnetic moment: 0 μ_B/Mn; $R_p = 21.5$, $R_{wp} = 18.7$, Bragg R factor: 7.58					
La(1)	2c	0.25	0.25	0.23178	1
Mn(1)	2b	0.75	0.25	0.5	0.77664
Sb(1)	2c	0.25	0.25	0.65623	1
Sb(2)	2a	0.75	0.25	0	1
$T = 80$ K					
Space group: $P4/nmm$; $a = b = 4.3704$ Å, $c = 10.7947$ Å; Magnetic moment: 2.353μ_B/Mn; $R_p = 23.5$, $R_{wp} = 20.1$, Bragg R factor: 8.22					
La(1)	2c	0.25	0.25	0.23126	1
Mn(1)	2b	0.75	0.25	0.5	0.77664
Sb(1)	2c	0.25	0.25	0.65564	1
Sb(2)	2a	0.75	0.25	0	1
$T = 3.5$ K					
Space group: $P4/nmm$; $a = b = 4.3686$ Å, $c = 10.7882$ Å; Magnetic moment: 3.276μ_B/Mn; $R_p = 25.5$, $R_{wp} = 21.6$, Bragg R factor: 10.16					
La(1)	2c	0.25	0.25	0.23206	1
Mn(1)	2b	0.75	0.25	0.5	0.77664
Sb(1)	2c	0.25	0.25	0.65597	1
Sb(2)	2a	0.75	0.25	0	1

for the low-field part of $\rho_{xy}(B)$ curves is 2.4×10^{22} cm^{-3} at room temperature [Fig. 4(d)], a slightly higher value than that in $A\mathrm{MnSb_2}$ (A = Sr, Ca, Yb) [18,19,27]. The dominant hole-type carrier is further evidenced by the positive Seebeck coefficient. As shown in Figs. 4(d) and 4(e), the behavior of the Seebeck coefficient curve is similar to that of hole concentration, which decreases upon cooling from room temperature to ∼ 50 K, and turns to increase with further cooling, forming a minimum at ∼ 50 K. Note that negative Seebeck coefficient is observed (21 ∼ 68 K), which is opposite to the sign of Hall resistivity. The difference in the sign of the Seebeck coefficient and Hall resistivity was usually interpreted in two scenarios, i.e., multiband effect and energy-dependent scattering time [31,32]. The interpretation with multiband effect is supported by the nonlinear Hall resistivity and band calculation in $\mathrm{LaMn_{0.86}Sb_2}$. For the multiband effect, the Seebeck coefficient of a two-band metal comprising both electron and hole can be expressed as [33]

$$S = \frac{\sigma_h|S_h| - \sigma_e|S_e|}{\sigma_h + \sigma_e} = \frac{n_h e\mu_h|S_h| - n_e e\mu_e|S_e|}{\sigma_h + \sigma_e}, \qquad (1)$$

where $\sigma = ne\mu$ is the electrical conductivity with carrier density n and mobility μ, the subscript $h(e)$ represents the contribution of the hole (electron) band. According to Eq. 1, the sign of the Seebeck coefficient is determined by both the carrier concentration and mobility. According to the first-principles calculation [Fig. 1(d)], both parabolic and Dirac linear bands cross the Fermi energy, forming hole-type and electron-type Fermi surfaces, respectively. As can be seen in Fig. 4(e), the contribution of electron carriers increases as the hole concentration decreases, and the sign change of the Seebeck coefficient occurs when the hole concentration reaches its minimum value. The electron-type Dirac linear band has higher mobility than hole bands with parabolic dispersion, which could lead to the sign change of the Seebeck coefficient in a compound still dominated by hole-type carriers. Because there are multiple Fermi surfaces with different dispersion as well as Mn vacancies induced spin disorder scatting in $\mathrm{LaMn_{0.86}Sb_2}$, the energy-dependent scattering time is also a possible explanation for the different signs between the Seebeck coefficient and Hall resistivity.

TABLE III. Basis vectors of the candidate irreducible representations (IR) Γ2, Γ5, Γ9, and Γ10, for the magnetic structure model on the 2b site of space group $P4/nmm$ with a propagation vector of $k = (0, 0, 1/2)$. The last column denotes whether the IR can be described by A or G types of AFM

IR	Basic vector		AFM type
	(x, y, z)	($-x$, y+1/2, $-z$)	
Γ_2	(0 0 1)	(0 0 −1)	A
Γ_5	(0 0 1)	(0 0 1)	G
Γ_9	(1 0 0) (0 −1 0)	(−1 0 0) (0 1 0)	A
Γ_{10}	(0 1 0) (−1 0 0)	(0 1 0) (−1 0 0)	G

Figure 4(f) displays the magnetic field dependence of magnetoresistance, MR(B), measured under various field orientations at 2 K, where MR is defined as MR(B) = $[\rho(B) - \rho(0)]/\rho(0) \times 100\%$. For $B \parallel c$, MR(B) shows a weak increase up to ∼ 2 T, then decreases steeply, forming a shoulder at ∼ 2 T which coincides with the spin-flop transition in $M(B)$ curves, indicating its magnetic origin. The MR eventually approaches saturation at the high magnetic field. The shoulder blurs as the magnetic field titles away from the c axis, and only a continuous decrease is observed when $\theta \geqslant 15^\circ$. The MR value at 2 K and 9 T is 9.8% for $B \parallel c$ and 11.4% for $B \perp c$.

The MR(B) measured at different temperatures for $B \parallel c$ and $B \perp c$ are plotted in Figs. 5(a) and 5(c), respectively. MR value decreases with increasing temperature for both $B \parallel c$ and $B \perp c$. The main feature for $\mathrm{MR}_\parallel(B)$ curves is that as the temperature increases the shoulder gradually shifts to a higher magnetic field and eventually becomes invisible above T_N, which can be better visualized by the first derivative of MR with respect to the magnetic field ($d\mathrm{MR}/dB$). The critical field for the spin-flop transition (B_{sf}) was defined as the peak of $d\mathrm{MR}/dB$, and the result is plotted in the magnetic phase diagram in Fig. 2(h), agreeing well with that determined from $M(B)$.

For an AFM metal, MR is theoretically predicted to be positive with the magnetic field applied along the easy axis

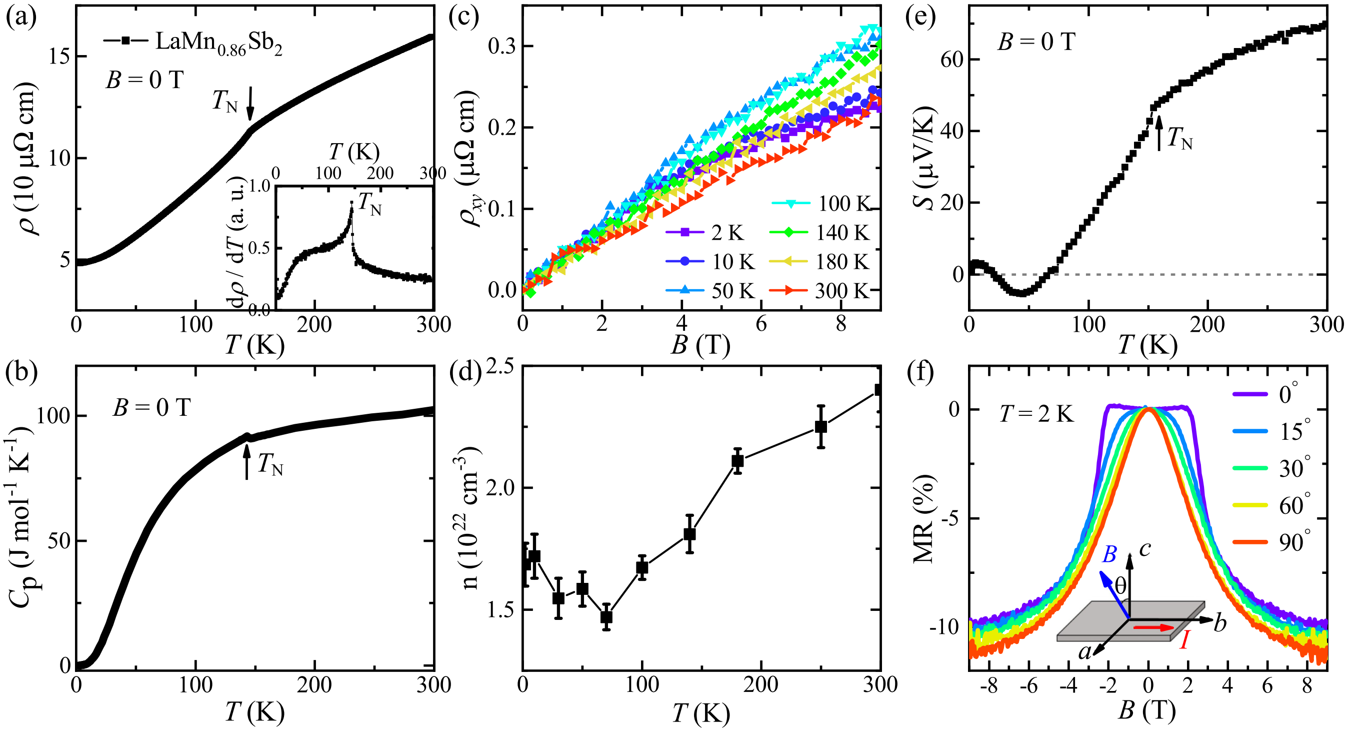

FIG. 4. (a) Temperature dependence of in-plane resistivity for a $\mathrm{LaMn_{0.86}Sb_2}$ single crystal; inset shows the first derivative of resistivity with respect to temperature $d\rho(T)/dT$. (b) Temperature dependence of specific heat $C_p(T)$ measured at $B = 0$ on the same single crystal. (c) Magnetic field dependence of Hall resistivity $\rho_{xy}(B)$ at different temperatures with $B \parallel c$. (d) Temperature dependence of carrier concentration extracted from the single-band fitting for $\rho_{xy}(B)$ in panel (c). (e) Seebeck coefficient as a function of temperature. (f) Magnetic field dependence of MR with field gradually titled away from c axis. Inset shows the configuration of the measurements, we cannot distinguish in-plane directions in our measurements.

while negligible positive value when the magnetic field is applied perpendicular to the easy axis [34]. $A\mathrm{MnSb_2}$ ($A =$ Sr, Ba, Eu, and Yb) exhibits a positive MR with quantum oscillation at a high magnetic field, and negative MR was only observed in semiconducting $\mathrm{EuMnSb_2}$ [5,7,9,18,20,21]. Negative MR is often observed in recently discovered intrinsic magnetic topological materials, such as $\mathrm{EuIn_2As_2}$, $\mathrm{EuCd_2P_2}$, $\mathrm{EuBiTe_3}$, $\mathrm{Eu_5In_2Sb_6}$, and $\mathrm{MnBi_2Te_4}$ [35–39]. The explanations for the negative MR in these magnetic topological materials can generally be classified into two physical mechanisms: spin alignment associated with spin scattering ($\mathrm{MnBi_2Te_4}$, $\mathrm{EuCd_2P_2}$) [36,39] and magnetic polaron associated with the phase separation ($\mathrm{EuIn_2As_2}$, $\mathrm{EuBiTe_3}$, and $\mathrm{Eu_5In_2Sb_6}$) [35,37,38]. Other mechanisms could also lead to negative MR, such as the chiral anomaly in Weyl semimetal [40], inhomogeneity of the sample [41], and current jetting [40]. For $\mathrm{LaMn_{0.86}Sb_2}$, the chiral anomaly is firstly excluded due to the transverse measurement configuration [see inset of Fig. 4(f)]. Current jetting can be rejected due to the large residual resistance. Although the inhomogeneity of $\mathrm{LaMn_{1-x}Sb_2}$ single crystal could be strong, it cannot explain the strong correlation with the magnetization. For the magnetic polaron mechanism, no evidence for the ferromagnetic cluster can be found at $T > T_N$. Moreover, the metallic resistivity, $d\rho(T)/dT > 0$, conflicts with the semiconducting resistivity, $d\rho(T)/dT < 0$, expected for the polaron hopping conduction [42,43]. Thus, the most likely mechanism for the negative MR in $\mathrm{LaMn_{0.86}Sb_2}$ is the spin alignment effect.

In the spin alignment scenario [44–46], MR is dominated by spin scattering, i.e., the interaction between itinerant spins and lattice spins. AFM coupling usually generates stronger spin disorder scattering than FM coupling, resulting in a high-resistivity state. With the magnetic field increasing, spin disorder scattering will decrease as the spins are gradually polarized to the field direction, resulting in negative MR. The spin alignment theory predicts that MR is closely correlated with magnetization [44–46], we, therefore, compare MR(B) with $M(B)$ in Fig. 5(d) to gain insight into their connection. $\mathrm{MR}_\parallel(B)$ exhibits a negligible positive value when the magnetization slowly increases as a function of the magnetic field. When $B > B_{sf}$, the steep decrease of $\mathrm{MR}_\parallel(B)$ is accompanied by the sharp increase of $M_\parallel(B)$, finally both $\mathrm{MR}_\parallel(B)$ and $M_\parallel(B)$ tend to saturation at the same time. $\mathrm{MR}_\perp(B)$ vs $M_\perp(B)$ exhibits a similar inversely correlation behavior.

To quantitatively reveal the correlation between MR(B) and $M(B)$, we try to fit MR vs M using the Majumdar-Littlewood (ML) model [47]:

$$|[\rho(B)-\rho(0)]/\rho(0)| \times 100\% \approx (1/2k_f\xi_0)^2(M/M_{\mathrm{sat}})^2, \quad (2)$$

where k_f is the Fermi momentum and ξ_0 is the correlation length. As shown in Fig. 5(e), we take $M_{\max}$ as M_{sat}, and find that $MR_\perp \propto (M/M_{\max})^{2.2}$, indicating the strong correlation between MR and magnetization. The ML model is consistent with the spin alignment mechanism [44,46,48]. Based on the

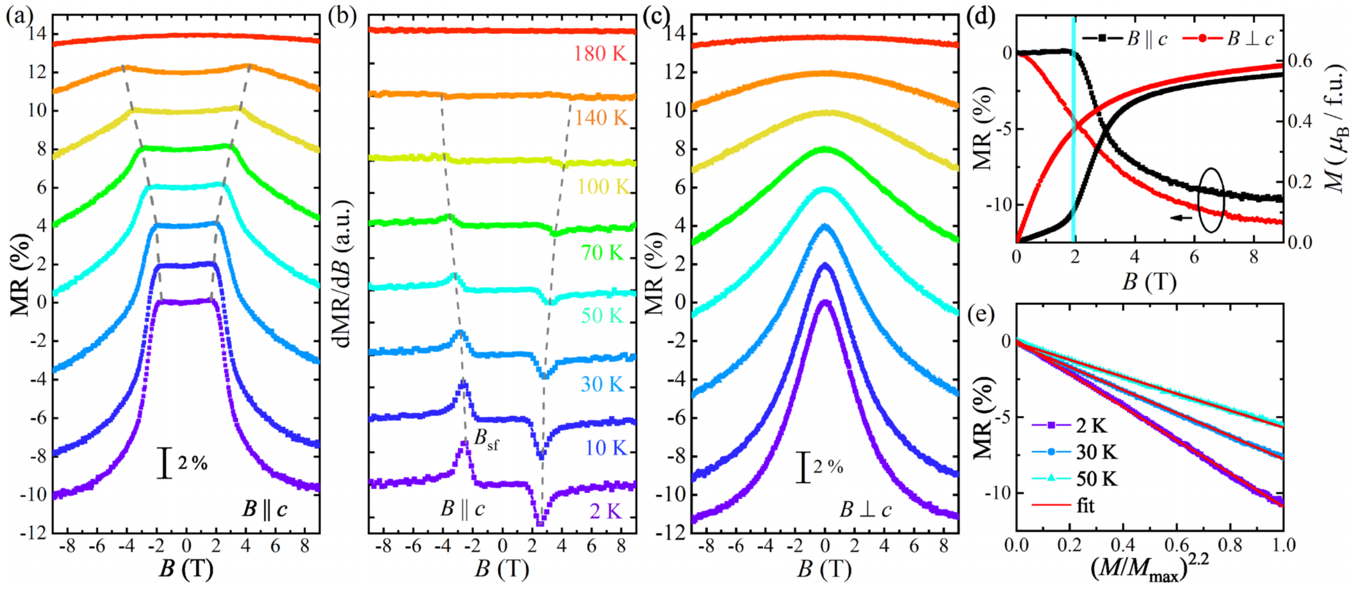

FIG. 5. Magnetic field dependence of MR for a $LaMn_{0.86}Sb_2$ single crystal at various temperatures with $B \parallel c$ (a) and $B \perp c$ (c). Each subsequent MR in (a) and (c) is shifted upward 2% for clarity. The dashed lines are guides to the eye. Panel (b) exhibits the first derivative of MR with respect to the magnetic field for $H \parallel c$. The dashed lines in (b) indicate the evolution of B_{sf}. Panels (a), (b), and (c) share the same legend, which is displayed in (b). Magnetic field dependence of MR (d, left panel) and magnetization (d, right panel) for $LaMn_{0.86}Sb_2$ at 2 K. The cyan line marks the spin-flop transition. (d) MR vs $(M/M_{max})^{2.2}$; red lines are linear fits.

analysis above, the negative MR in $LaMn_{0.86}Sb_2$ can be explained in terms of the spin alignment effect.

IV. CONCLUSION

In conclusion, we successfully grew out $LaMn_{0.86}Sb_2$ single crystals using the flux method. There are 14% Mn vacancies in $LaMn_{0.86}Sb_2$ single crystals. Based on the magnetization and neutron diffraction measurements, the magnetic structure of $LaMn_{0.86}Sb_2$ is very likely a canted G-type AFM. The negative magnetoresistance arising from the spin alignment effect is observed. Although the first-principles calculation indicates the presence of Dirac dispersion below the Fermi level, the relevant quantum transport properties have not been observed due to the high Fermi energy and the existence of Mn vacancy. Our results indicate that $LaMn_{1-x}Sb_2$ has a vacancy tunable magnetism and Dirac dispersion, which could be an interesting topological semimetal candidate via proper adjusting of the Fermi energy and Mn vacancies. Further studies of putative Dirac states and their interaction with magnetism are of high interest.

ACKNOWLEDGMENTS

We acknowledge helpful discussions with C. Petrovic, Z. Xiang, Y. Song, S. Cui, and E. Feng. This work was financially supported in part by the National Natural Science Foundation of China (Grants No. 12004056, No. 52071323, No. 11904040, No. 11974065, No. 12104072, and No. 52071041), Chongqing Research Program of Basic Research and Frontier Technology, China (Grants No. cstc2021jcyj-msxmX0661, No. cstc2020jcyj-msxmX0263, and No. cstc2021jcyj-msxmX0640), Fundamental Research Funds for the Central Universities, China (Grant No. 2022CDJXY-002), the Venture and Innovation Support Program for Chongqing Overseas Returnees (Grant No. cx2021050), and the Doctor "Through train" Scientific Research Project of Chongqing (Grant No. CSTB2022BSXM-JCX0087). We would like to thank G. Wang, B. Zhang, and Y. Liu at the Analytical and Testing Center of Chongqing University for their assistance with measurements. We acknowledge ANSTO for neutron beam time. Numerical computations were performed on Hefei advanced computing center.

---

[1] S. Klemenz, S. Lei, and L. M. Schoop, Annu. Rev. Mater. Res. **49**, 185 (2019).

[2] G. Lee, M. A. Farhan, J. S. Kim, and J. H. Shim, Phys. Rev. B **87**, 245104 (2013).

[3] J. Park, G. Lee, F. Wolff-Fabris, Y. Y. Koh, M. J. Eom, Y. K. Kim, M. A. Farhan, Y. J. Jo, C. Kim, J. H. Shim, and J. S. Kim, Phys. Rev. Lett. **107**, 126402 (2011).

[4] H. Masuda, H. Sakai, M. Tokunaga, Y. Yamasaki, A. Miyake, J. Shiogai, S. Nakamura, S. Awaji, A. Tsukazaki, H. Nakao *et al.*, Sci. Adv. **2**, e1501117 (2016).

[5] L. Zhang, Z. Sun, A. Wang, Y. Xia, X. Mi, L. Zhang, M. He, Y. Chai, T. Wu, R. Wang *et al.*, Phys. Rev. B **104**, 205108 (2021).

[6] S. Borisenko, D. Evtushinsky, Q. Gibson, A. Yaresko, K. Koepernik, T. Kim, M. Ali, J. van den Brink, M. Hoesch, A. Fedorov *et al.*, Nat. Commun. **10**, 3424 (2019).

[7] J. Y. Liu, J. Hu, Q. Zhang, D. Graf, H. B. Cao, S. M. A. Radmanesh, D. J. Adams, Y. L. Zhu, G. Cheng, X. Liu *et al.*, Nat. Mater. **16**, 905 (2017).

[8] J. Y. Liu, J. Yu, J. L. Ning, H. M. Yi, L. Miao, L. J. Min, Y. F. Zhao, W. Ning, K. A. Lopez, Y. L. Zhu *et al.*, Nat. Commun. **12**, 4062 (2021).

[9] Z. L. Sun, A. F. Wang, H. M. Mu, H. H. Wang, Z. F. Wang, T. Wu, Z. Y. Wang, X. Y. Zhou, and X. H. Chen, npj Quantum Mater. **6**, 94 (2021).

[10] O. Sologub, K. Hiebl, P. Rogl, and O. Bodak, J. Alloys Compd. **227**, 40 (1995).

[11] P. Wollesen, W. Jeitschko, M. Brylak, and L. Dietrich, J. Alloys Compd. **245**, L5 (1996).

[12] See Supplemental Material at http://link.aps.org/supplemental/10.1103/PhysRevB.107.115150 for XRD, magnetotransport, and magnetization data of $\mathrm{LaMn}_{1-x}\mathrm{Sb}_2$ with $x = 0$, 0.14, and 0.16

[13] M. Avdeev and J. R. Hester, J. Appl. Crystallogr. **51**, 1597 (2018).

[14] G. Kresse and J. Furthmüller, Phys. Rev. B **54**, 11169 (1996).

[15] G. Kresse and J. Furthmüller, Comput. Mater. Sci. **6**, 15 (1996).

[16] J. P. Perdew, K. Burke, and M. Ernzerhof, Phys. Rev. Lett. **77**, 3865 (1996).

[17] P. E. Blöchl, Phys. Rev. B **50**, 17953 (1994).

[18] Y.-Y. Wang, S. Xu, L.-L. Sun, and T.-L. Xia, Phys. Rev. Mater. **2**, 021201(R) (2018).

[19] J. B. He, Y. Fu, L. X. Zhao, H. Liang, D. Chen, Y. M. Leng, X. M. Wang, J. Li, S. Zhang, M. Q. Xue, C. H. Li *et al.*, Phys. Rev. B **95**, 045128 (2017).

[20] S. Huang, J. Kim, W. A. Shelton, E. W. Plummer, and R. Jin, Proc. Natl. Acad. Sci. USA **114**, 6256 (2017).

[21] C. Yi, S. Yang, M. Yang, L. Wang, Y. Matsushita, S. Miao, Y. Jiao, J. Cheng, Y. Li, K. Yamaura, Y. Shi, and J. Luo, Phys. Rev. B **96**, 205103 (2017).

[22] M. A. Farhan, G. Lee, and J. H. Shim, J. Phys.: Condens. Matter **26**, 042201 (2014).

[23] R. Kealhofer, S. Jang, S. M. Griffin, C. John, K. A. Benavides, S. Doyle, T. Helm, P. J. W. Moll, J. B. Neaton, J. Y. Chan *et al.*, Phys. Rev. B **97**, 045109 (2018).

[24] S. K. Malik, Z. Chu, A. G. Joshi, J. B. Yang, W. B. Yelon, Q. Cai, W. J. James, and K. Kamaraju, J. Appl. Phys. **91**, 7842 (2002).

[25] Y. Takahashi, T. Urata, and H. Ikuta, Phys. Rev. B **104**, 054408 (2021).

[26] A. Wang, I. Zaliznyak, W. Ren, L. Wu, D. Graf, V. O. Garlea, J. B. Warren, E. Bozin, Y. Zhu, and C. Petrovic, Phys. Rev. B **94**, 165161 (2016).

[27] Y. Liu, T. Ma, L. Zhou, W. E. Straszheim, F. Islam, B. A. Jensen, W. Tian, T. Heitmann, R. A. Rosenberg, J. M. Wilde *et al.*, Phys. Rev. B **99**, 054435 (2019).

[28] J.-R. Soh, S. M. Tobin, H. Su, I. Zivkovic, B. Ouladdiaf, A. Stunault, J. A. Rodríguez-Velamazán, K. Beauvois, Y. Guo, and A. T. Boothroyd, Phys. Rev. B **104**, L161103 (2021).

[29] Y. F. Guo, A. J. Princep, X. Zhang, P. Manuel, D. Khalyavin, I. I. Mazin, Y. G. Shi, and A. T. Boothroyd, Phys. Rev. B **90**, 075120 (2014).

[30] Q. Zhang, J. Liu, H. Cao, A. Phelan, D. Graf, J. F. DiTusa, D. A. Tennant, and Z. Mao, NPG Asia Mater. **14**, 22 (2022).

[31] K. Wang and C. Petrovic, Phys. Rev. B **86**, 155213 (2012).

[32] B. Xu and M. J. Verstraete, Phys. Rev. Lett. **112**, 196603 (2014).

[33] R. D. Barnard, *Thermoelectricity in Metals and Alloys* (Taylor & Francis Group, London, 1972).

[34] H. Yamada and S. Takada, J. Phys. Soc. Jpn. **34**, 51 (1973).

[35] Y. Zhang, K. Deng, X. Zhang, M. Wang, Y. Wang, C. Liu, J.-W. Mei, S. Kumar, E. F. Schwier, K. Shimada *et al.*, Phys. Rev. B **101**, 205126 (2020).

[36] Z. Wang, J. D. Rogers, X. Yao, R. Nichols, K. Atay, B. Xu, J. Franklin, I. Sochnikov, P. J. Ryan, D. Haskel, and F. Tafti, Adv. Mater. **33**, 2005755 (2021).

[37] W. Shon, J.-S. Rhyee, Y. Jin, and S.-J. Kim, Phys. Rev. B **100**, 024433 (2019).

[38] P. Rosa, Y. Xu, M. Rahn, J. Souza, S. Kushwaha, L. Veiga, A. Bombardi, S. Thomas, M. Janoschek, E. Bauer *et al.*, npj Quantum Mater. **5**, 52 (2020).

[39] J. Cui, M. Shi, H. Wang, F. Yu, T. Wu, X. Luo, J. Ying, and X. Chen, Phys. Rev. B **99**, 155125 (2019).

[40] S. Liang, J. Lin, S. Kushwaha, J. Xing, N. Ni, R. J. Cava, and N. P. Ong, Phys. Rev. X **8**, 031002 (2018).

[41] J. Hu, M. M. Parish, and T. F. Rosenbaum, Phys. Rev. B **75**, 214203 (2007).

[42] S. Pal, A. Banerjee, E. Rozenberg, and B. K. Chaudhuri, J. Appl. Phys. **89**, 4955 (2001).

[43] P. Majumdar and P. Littlewood, Phys. Rev. Lett. **81**, 1314 (1998).

[44] P. G. De Gennes and J. Friedel, J. Phys. Chem. Solids **4**, 71 (1958).

[45] H. Diep, Y. Magnin, and D.-T. Hoang, Acta Phys. Pol. A **121**, 985 (2012).

[46] C. Haas, Phys. Rev. **168**, 531 (1968).

[47] P. Majumdar and P. B. Littlewood, Nature (London) **395**, 479 (1998).

[48] I. Karla, J. Pierre, and R. Skolozdra, J. Alloys Compd. **265**, 42 (1998).